LA-UR-24-31839
Accepted Manuscript

Spectroscopy of the Hamburg Meteorite, Michigan H4

Dyar, M.D.; Breitenfeld, Laura B; Lane, Melissa D; Glotch, Timothy D.; Clark, Roger; Pearson, Neil; Sklute, Elizabeth Christ; Hendrix, Amanda J; Weller, Brandon; Schaller, Morgan; Kling, Alexander; McDougall, Dylan

Provided by the author(s) and the Los Alamos National Laboratory (1930-01-01).

To be published in: The Planetary Science Journal

DOI to publisher's version: 10.3847/PSJ/ae0a4f

Permalink to record:
https://permalink.lanl.gov/object/view?what=info:lanl-repo/lareport/LA-UR-24-31839

Los Alamos National Laboratory, an affirmative action/equal opportunity employer, is operated by Triad National Security, LLC for the National Nuclear Security Administration of U.S. Department of Energy under contract 89233218CNA000001. By approving this article, the publisher recognizes that the U.S. Government retains nonexclusive, royalty-free license to publish or reproduce the published form of this contribution, or to allow others to do so, for U.S. Government purposes. Los Alamos National Laboratory requests that the publisher identify this article as work performed under the auspices of the U.S. Department of Energy. Los Alamos National Laboratory strongly supports academic freedom and a researcher's right to publish; as an institution, however, the Laboratory does not endorse the viewpoint of a publication or guarantee its technical correctness.

The Planetary Science Journal, 6:240 (13pp), 2025 October https://doi.org/10.3847/PSJ/ae0a4f
© 2025. The Author(s). Published by the American Astronomical Society.
OPEN ACCESS

Spectroscopy of the Hamburg Meteorite, Michigan H4

M. Darby Dyar[1,2], Laura B. Breitenfeld[1,2], Melissa D. Lane[3], Timothy Glotch[4], Roger Clark[1], Neil Pearson[1], Elizabeth C. Sklute[1,2,5], Molly C. McCanta[6], Amanda J. Hendrix[1], Brandon Weller[7], Morgan Schaller[8], Alexander Kling[4,9], and Dylan McDougall[10]

[1] Planetary Science Institute, 1700 East Fort Lowell, Suite 106, Tucson, AZ 85719, USA; mdyar@psi.edu
[2] Department of Astronomy, Mount Holyoke College, 50 College Street, South Hadley, MA 01075, USA
[3] Fibernetics LLC, Lititz, PA 17543, USA
[4] Department of Geosciences, 255 Earth and Space Science Building, Stony Brook, NY 11794, USA
[5] Los Alamos National Laboratory, PO Box 1663, MSB244, Los Alamos, NM 87544, USA
[6] Department of Earth and Planetary Sciences, University of Tennessee, Knoxville, TN 37996, USA
[7] Rutgers NJMS, Department of Ophthalmology, 90 Bergen Street, Newark, NJ 07103, USA
[8] Department of Earth and Environmental Science, Rensselaer Polytechnic Institute, 110 Eighth Street, Troy, NY 12180, USA
[9] Department of Earth, Atmospheric, and Planetary Sciences, Purdue University, West Lafayette, IN 47907, USA
[10] Nicholas School of the Environment, Duke University, 9 Circuit Drive, Box 90328, Durham, NC 27708, USA
Received 2024 November 7; revised 2025 July 7; accepted 2025 September 18; published 2025 October 24

Abstract

Spectroscopic studies of the Hamburg (Michigan H4) meteorite using visible–near-infrared (VNIR), mid-infrared (MIR), Raman, and Mössbauer data reproduce the results of more conventional laboratory measurements of petrology and geochemistry. This combination provides general information on the mineral modes of silicates, although spectroscopy was performed on different splits of this meteorite, and varying results may be explained by heterogeneity that is typical of ordinary chondrites. Raman also detects small features assigned to first-order D and G carbon bands, while Mössbauer data show the presence of Fe oxides and carbides. The electron microprobe (EMPA) composition of olivine in this meteorite is accurately measured to be $Fo_{81.3}$, while MIR and Raman closely agree with Fo_{80} and Fo_{82}, respectively, and Mössbauer, at $Fo_{60} - Fo_{70}$, is in the ballpark. Similarly, P. R. Heck et al. report pyroxenes with compositions of $Fs_{16}Wo_1$, while Raman suggests a somewhat similar composition of $Fs_{28}Wo_0$. Both VNIR and MIR detect the presence of small amounts of feldspar, while EMPA identifies its composition as $An_{14}Ab_8Or_5$. VNIR data were matched to spectral libraries of meteorite and asteroid data and shown to closely match other L and H meteorites. The best spectral matches to the Michigan H4 meteorite are to asteroid classes L/H/LL/URE, EH/EL/AUB, and CO/CV from M. D. Dyar et al.; objects in this group are intermediate in semimajor axis lengths for their orbits. The results highlight the strengths and weaknesses of each technique and show their collective strength when applied together to a single meteorite sample.

Unified Astronomy Thesaurus concepts: Carbonaceous chondrites (200); Asteroid belt (70); Electronic spectroscopy (2247); Gamma-ray spectroscopy (2283)

1. Introduction

Since it fell on 2018 January 17, the Hamburg (Michigan H4) meteorite has been the subject of intense public and scientific interest. Because many fragments were recovered, it provides an unusual opportunity to study a chondrite fall with minimal alteration and sufficient mass for characterization using a variety of spectroscopic techniques. This study presents visible–near-infrared (VNIR), mid-infrared (MIR), Raman, and Mössbauer data measured on the interior and crust of the meteorite. This paper supplements the otherwise exhaustive characterization of this meteorite by the community (e.g., P. G. Brown et al. 2019; P. R. Heck et al. 2020) and suggests possible spectral parent-body matches for this meteorite. It also provides an opportunity to compare and contrast results from remote spectroscopic methods that might be deployed on a mission to an asteroid body.

Modern geochemistry offers a wide variety of analytical techniques to geoscientists, many of which require increasingly specialized tools, interpretations, and practitioners. Moreover, planetary exploration using varying combinations of landers and remote instrumentation also is becoming more common (for example, on the Moon and Mars). As a result, there is a need to better understand how complementary analytical methods can confirm results from individual techniques. In addition, the extensive laboratory work on Michigan H4 offers an opportunity to contrast the science that is possible from returned samples versus remote measurements. This paper offers an opportunity to bring multiple techniques to bear on the study of an already well-characterized meteorite, the Hamburg Michigan H4 chondrite.

2. Background

Several aspects of this meteorite's fall near Hamburg, Michigan, and subsequent handling are already reported in the literature, so they need only to be summarized here. M. A. H. Hedlin et al. (2018) report the use of optical sensors, regional infrasonic microphones, and seismometers to document the location and timing of the impact. M. Fries et al. (2019) present a simulation of the cold curation procedures used. J. L. Mitchell et al. (2020) describe the use of bioswabs to determine species found on the samples, further

Original content from this work may be used under the terms of the Creative Commons Attribution 4.0 licence. Any further distribution of this work must maintain attribution to the author(s) and the title of the work, journal citation and DOI.

characterizing terrestrial contamination. P. G. Brown et al. (2019) summarize the fireball trajectory, orbit, and dynamics.

Most germane to this paper is the work of P. R. Heck et al. (2020), who provide details on the fall, recovery, classification, magnetic properties, petrology, and geochemistry of this meteorite but do not use spectroscopic techniques. They note that most of the stones recovered from this fall are covered in fusion crust—thus, the sample studied here with spectroscopy is typical. Some samples show staining and rusty weathering on the surfaces, which is interpreted as a sign of terrestrial weathering, despite their quick collection. Samples contain roughly 9% metal, with a composition of 6.6 wt% Ni and 0.55 wt% Co; P, Cr, Mn, and S in the metal are all below detection. Abundant chondrules are observed in samples studied by P. R. Heck et al. (2020). Most are porphyritic olivine chondrules with pyroxene; radial pyroxene and barred olivine chondrules are also present.

Olivine, orthopyroxene (opx), clinopyroxene (cpx), phosphates, and chromite compositions from our sample resemble those analyzed by P. R. Heck et al. (2020). The individual phases are quite chemically homogeneous. Olivine is consistently $Fo_{81.3 \pm -0.7}$ in the Heck "type" specimen. Low-Ca pyroxene (opx) falls within a range from $Fs_{15.9}$ to $Fs_{20.2}$ and averaged $Fs_{16.3 \pm 0.4}Wo_{1.3 \pm 0.3}$. Microphenocrysts of low-Ca pyroxene and olivine show some slight zoning near the edges of porphyritic chondrules, with compositions ranging up to $Fo_{73.7–96.0}$ and $Fs_{0.1–20.2}$. Feldspar in the type specimen has an average composition of $An_{14.0 \pm 4.0}Ab_{81.1 \pm 3.0}Or_{4.8 \pm 1.3}$. Other phases detected by P. R. Heck et al. (2020) include trace phosphates (merrillite and apatite, isolated chromite, ilmenite, and melt veins comprised of Fe sulfide). Aside from estimated abundances of phosphates (trace) and metal (∼7%), no modal abundances have been reported for this sample.

Other geochemical characteristics reported in P. R. Heck et al. (2020) include a cosmic-ray exposure age of ∼12 Ma for a 40–60 cm diameter meteoroid. The ^{40}Ar-^{39}Ar age of 4532 ± 24 Ma is consistent with other H4 chondrites and with Pb-Pb ages of 4549 ± 36 Ma (LA-ICPMS) and 4535.3 ± 9.5 Ma (SIMS) in phosphates and a U-Pb Concordia age of 4535 ± 10 Ma.

3. Provenance

The sample used for our analyses (Figure 1) was found by an undergraduate citizen scientist (B.W.) using weather radar data collected by NEXRAD as well as the Terminal Doppler Weather Radar short-range weather radar for the Detroit airport. The meteorite was collected by B.W. 3 days after the fall on 2018 January 19 at 42°27′07″N, 83°51′01″W. The piece is a 59.4 g oriented stone fully coated with a fusion crust that was found on the frozen surface of Strawberry Lake. Interestingly, the piece was indented approximately 2 cm into the snow and partially fused with the ice below, possibly secondary to solar thermal heating/cooling cycles.

The sample is mildly brecciated, and four distinct fragments could be seen separated by two primary fractures. The sample was cut with a water-lubricated saw and immediately placed in an oven for gentle drying for 1 hr. This sample never touched epoxy. The hand sample interior is mostly gray but appears to have minor iron staining on various phases. It is unknown if this oxidation resulted from sitting on the ground for the 3 days before it was collected, or if this staining is intrinsic to the meteorite (M. A. Velbel 2014). Some crumbling did occur during preparation of the slab; the largest piece was ∼2 mm thick and ∼1 cm long (Figure 1), weighing ∼0.5 g. The fragments were eventually crushed for powder spectroscopy, and some analyses were made of the slab as described above. Note that a separate sample was prepared as a 1 inch round polished mount for microanalysis.

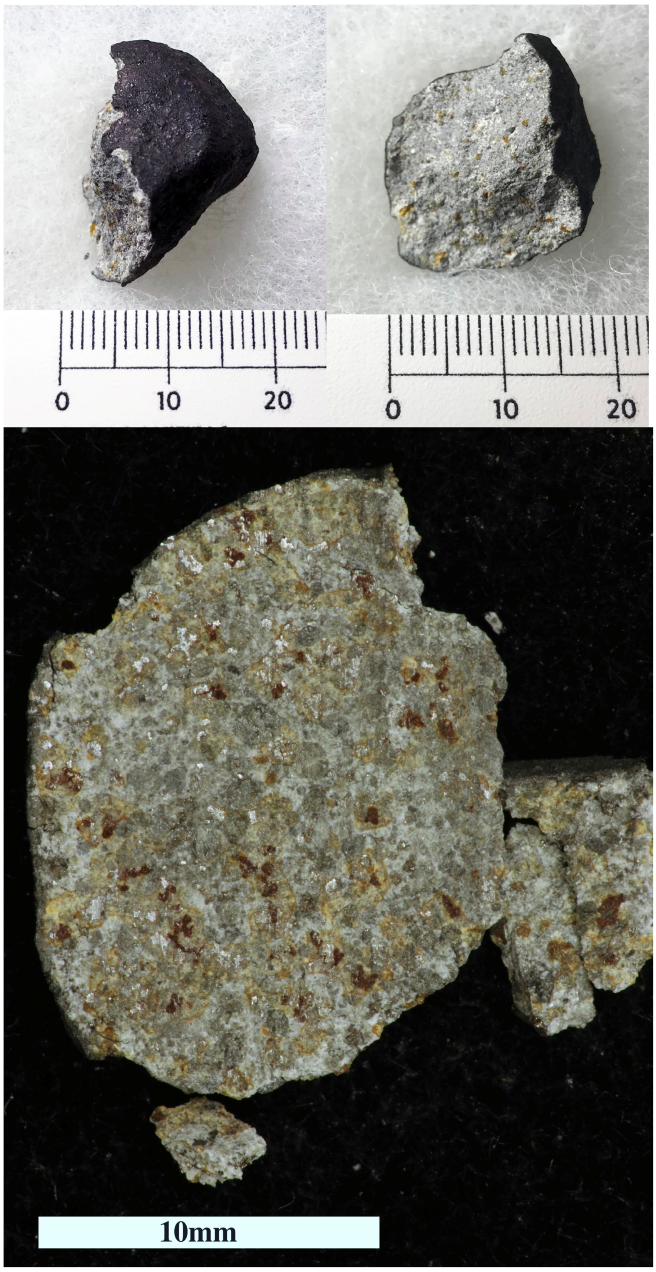

Figure 1. (Top) Sample cut for this study. Photos by B.W. Some crumbles were produced while slabbing this sample, and those loose pieces were handpicked into aliquots from the crust vs. the interior for use in spectroscopy. (Bottom) Chip loaned by Mike Farmer for VNIR studies.

An additional sample studied was a slab loaned to the Planetary Science Institute (PSI) by Mike Farmer. The small slice of meteorite is approximately 10 mm by 15 mm. The overall coloring is light gray. There are visible chondrules mostly well formed with defined edges. Iron nickel is also present along with dark red blebs of possibly oxidized iron or iron sulfide.

4. Methods

4.1. VNIR Reflectance and Shortwave Infrared Spectroscopy

We analyzed two samples of the Hamburg meteorite: a sawed slab and a powder. In this range, the slab showed a better signal-to-noise ratio than the powder, and the following interpretation is of the spectrum of the slab only.

The 0.35–2.5 μm data were obtained with an Analytical Spectral Devices (ASD) Fieldspec3 with an FWHM spectral resolution of 3 nm at 0.7 μm and 10 nm at 1.4 and 2.1 μm, using 2151 channels. These spectral resolutions correspond to the three different detectors used in the spectrometer, a silicon detector covering 0.35–1.0 μm and two indium gallium arsenide detectors covering the wavelength ranges 1.0–1.8 μm and 1.8–2.5 μm. The light source for measurements was a quartz-tungsten halogen bulb at an incidence of 0°. Reflected sample light was collected by a fiber optic bundle at a 30° emission angle and transmitted to the detectors. Reflectance measurements were taken relative to a Labsphere Spectralon panel, and the absolute reflectance of Spectralon was used to correct the Hamburg data to absolute bidirectional reflectance using the methods described in R. N. Clark et al. (1990) and R. F. Kokaly et al. (2017). Spectralon has several percent spectral structure beyond 2 μm, and a sample divided by Spectralon reflectance would result in upward bumps in the spectrum relative reflectance. Multiplying the sample or Spectralon spectrum by the absolute reflectance of Spectralon removes the residual Spectralon signatures.

The 2.5–6.5 μm data were taken with an Agilent 4300 handheld Fourier transform infrared spectrometer (FTIR) equipped with a diffuse reflectance sampling module and a deuterated triglycene sulfate detector. Although data were acquired by the Agilent 4300 out to 15 μm, we are not presenting the 6.5–15 μm data in favor of better bench-top MIR data (below). Data were taken relative to a diffuse gold standard at 8 cm^{-1} spectral resolution. An incidence angle of 0° and emission angle of 45° were used to achieve a phase angle of 45°.

4.2. MIR (aka Thermal, Vibrational) Emission Spectroscopy

A 59.4 g chunk of the meteorite with a fusion crust and an exposed interior was measured at Stony Brook University's Center for Planetary Exploration (CPEX) to acquire the MIR emission spectra of the meteorite interior (under ambient pressure and then under simulated asteroid environment, SAE, conditions) and exterior (fusion crust) under SAE conditions. The rough, broken-surface meteorite interior sample spectrum measured under ambient pressure was acquired using a Nicolet Nexus 6700 FTIR. It has been modified for emission measurements by removal of the Globar source and placement of an enclosed glove box and folding mirrors outside the spectrometer housing to enable the energy from a heated sample in a double-walled copper sample chamber to enter into the ray path for measurement. The chamber wall is water-cooled to maintain the environmental temperature. The atmosphere within the spectrometer and sample chamber was scrubbed of CO_2 and H_2O to reduce their spectral lines in the sample data. The spectrometer is equipped with a KBr beam splitter and a deuterated L-alanine doped tryglycine sulfate (DLaTGS) detector that allows quality measurement of emitted radiation over the MIR range of 2000–400 cm^{-1} (5–25 μm). For the measurement, the meteorite was heated in an oven maintained at an 80°C set point, and the hot meteorite was placed into the spectrometer in the water-cooled environmental chamber for the duration of the measurement, gradually cooling throughout the experiment. The 240 scans of each sample were acquired at 4 cm^{-1} spectral resolution (2 cm^{-1} spectral sampling), and the individual scan spectra were averaged together.

Two blackbody target measurements (at ~70°C and 100°C) also were obtained to determine the instrument response function and instrument temperature used for calibration. The emissivity spectrum of the meteorite was derived by reducing the raw wavelength- and temperature-dependent data by conversion of the sample's raw voltage data measured at the detector into calibrated sample radiance by dividing the voltage by the instrument response function, then dividing this sample radiance curve into the temperature-appropriate Planck blackbody curve. The result is (unitless) sample emissivity that ranges from 0 to 1.0 (a blackbody would present an emissivity of 1.0 across the wavelength range). The resulting sample spectrum was calibrated according to the procedure discussed in detail in S. W. Ruff et al. (1997) and converted to spectral emissivity.

SAE spectra of the meteorite interior and exterior samples were acquired in the Planetary and Asteroid Regolith Spectroscopy Environment Chamber (PARSEC) at CPEX (K. A. Shirley & T. D. Glotch 2019; L. B. Breitenfeld et al. 2021; K. A. Shirley et al. 2023). SAE conditions are achieved by pumping the chamber down to a pressure of $<10-5$ mbar, heating the samples from below to 80°C, heating from above via a 75 W quartz halogen lamp connected to a tunable power source, and cooling the chamber to <-123°C via input of liquid nitrogen into an internal dewar. PARSEC is connected to a Nicolet 6700 FTIR spectrometer equipped with a KBr beam splitter and a DLaTGS detector with a KBr window.

Blackbody spectra at 70°C and 100°C were acquired subsequent to the collection of each sample spectrum and used to calibrate and process the sample spectra to emissivity as for the ambient condition measurements.

4.3. Raman Spectroscopy

From the chunk analyzed for MIR, two particulate splits were made, one from the interior portion of the meteorite and one from the crust. Raman spectra were acquired on a Bruker Senterra II instrument using a 532 nm laser and 12.5 mW power. The spectra were acquired with 10 (interior) and 20 (crust) s of integration time and multiple sample scans. The highest Senterra spectral resolution available of 0.5 cm^{-1} $channel^{-1}$ was utilized. Raman peak positions were determined by fitting each feature with a Gaussian curve and extracting the fit parameters. The two powder splits were then sent to Tucson for VNIR and shortwave infrared (SWIR) measurements.

Two methodologies for mineral quantification using Raman spectroscopy were undertaken: multivariate models and Raman cross-section proxies (L. B. Breitenfeld et al. 2025). Mineral abundance predictions for olivine (forsterite) and pyroxene (enstatite) were emphasized because those are the minerals identified through this technique and available as models from L. B. Breitenfeld et al. (2025). For both quantification techniques, the meteorite interior spectrum was cropped to a reduced spectral range (300–1500 cm^{-1}), baseline-corrected using AirPLS software (smoothness set to 100),

and normalized. Multivariate models employed partial least squares for prediction of the modal mineralogy of the meteorite. For the Raman cross-section proxy method, Raman bands were peak fitted using Gaussian fits to determine the feature areas from the diagnostic olivine ($\sim$852 cm^{-1}) and pyroxene ($\sim$1008 cm^{-1}) peaks. Next, the peak areas and Raman cross-section proxy values in Equation (2) of L. B. Breitenfeld et al. (2025) were used to derive quantitative mineralogy.

4.4. Mössbauer Spectroscopy

After VNIR measurements were made at PSI, the two particulate splits were returned to Massachusetts. Approximately 40 mg of fusion crust and interior were crushed under acetone, then mixed with a sugar–acetone solution designed to form sugar coatings around each grain and prevent preferred orientation during measurement. The amount of sample used was determined by the amount available. Grains were heaped gently in a sample holder confined by Kapton® tape. Mössbauer spectra were acquired using a source of $\sim$40 mCi ^{57}Co in Rh on a WEB Research Co. model WT302 spectrometer (housed at Mount Holyoke College) equipped with a scintillation detector. Spectra were acquired at 293 K.

Runtimes were 36 hr, and baseline counts ranged from $\sim$10 to 20 million after the folding and the Compton correction (see M. D. Dyar et al. 2009 for details), as needed to obtain reasonable counting statistics. Spectra were collected in 2048 channels and corrected for nonlinearity via interpolation to a linear velocity scale, which is defined by the spectrum of the 25 μm thick Fe foil used for calibration. To model the data, we used a custom program generously made available to us by Eddy DeGrave and Toon VanAlboom at the University of Ghent, in Belgium, called MexfielDD, which is well suited to modeling highly overlapped spectra. MexfielDD was used to provide Lorentzian line shapes and the capability of solving the full hyperfine interaction Hamiltonian. Quadrupole splitting (Δ), center shift (δ, referenced to α-Fe), and line width were generally allowed to vary freely, though some constraints on δ and Δ were used to model the very small doublets representing Fe^{3+} and other impurities. Areas were allowed to vary in pairs (e.g., the areas of peaks 1 and 4 were allowed to vary in unison, and the areas of peaks 2 and 3 were allowed to vary together).

Errors on center shifts and quadrupole splitting are estimated at better than $\pm$0.02 mm s^{-1}. The distribution of area between coexisting Fe^{2+} doublets is nonunique, and probably $\pm$5%–10% absolute, but the summed areas of the smaller (e.g., Fe^{3+}) components relative to the total area are accurate to within $\pm$1%–3% absolute.

4.5. Classification and Matching

The VNIR spectra obtained in this study were matched to a database developed by M. D. Dyar et al. (2023) for the purpose of classifying asteroids on the basis of their spectral similarities to meteorites. The database includes 1422 meteorite spectra representing 20 classes. The data cover the range from 0.3 to 2.6 μm in increments of either 0.005 or 0.01 μm and were cropped to match the 0.35–2.5 μm data from PSI. The asteroid data were a mixture of spectra from SMASS (F. E. DeMeo et al. 2009) and the MIT-Hawaii Near-Earth Object Spectroscopic Survey (MITHNEOS; R. P. Binzel et al. 2019). The MITHNEOS data set includes both near-Earth asteroids and Mars-crossers. The SMASS spectra range from 0.45 to 2.45 μm in increments of 0.005 μm, while the MITHNEOS data (taken from a variety of sources) range from $\sim$0.4 to $\sim$2.45 μm in increments of $\sim$0.005 μm.

Matching was undertaken using the whole spectrum L1/cosine mixture approach described in C. Carey et al. (2015) as implemented on the Data Exploration and Visualization for Spectroscopy website at Mount Holyoke College.[11]

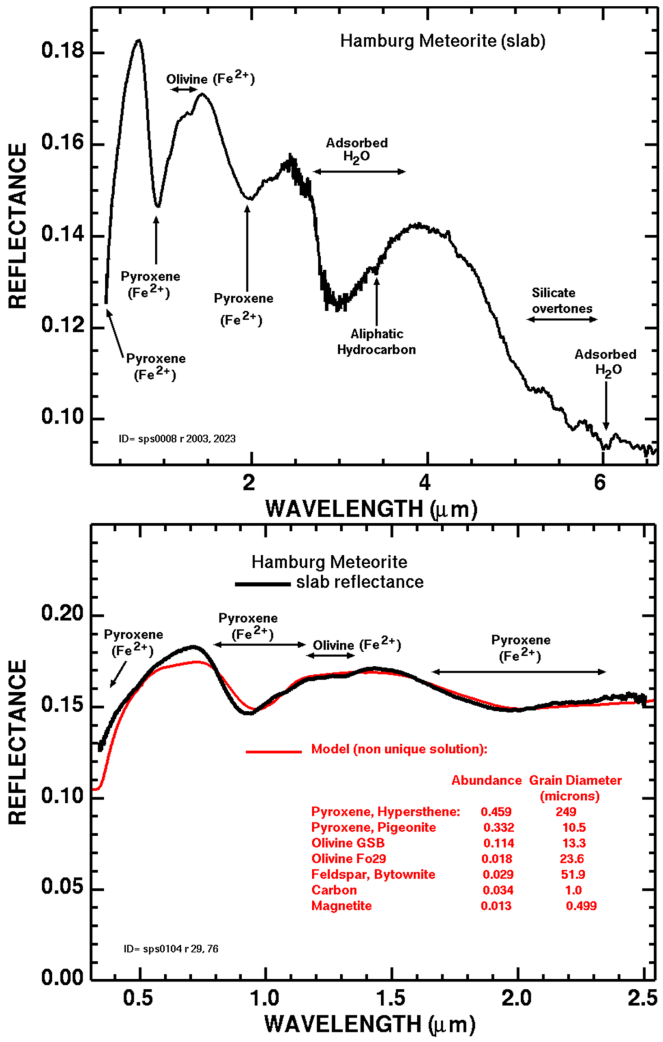

Figure 2. (Top) Spectrum of the meteorite slab showing characteristic features. Data are combined at 2.5 μm, with shortward being from ASD and longward being Agilent spectra. (Bottom) Reflectance model fit (red line) to the reflectance spectrum of a Hamburg meteorite slab (black line). Abundances are given in wt%.

5. Results

5.1. VNIR and SWIR

The combined VNIR–SWIR spectrum (0.35–6.5 μm) is shown in Figure 2 (top) with features labeled. The spectrum of the slab shows a VNIR reflectance between about 12% and 18%, brighter than the powder with reflectance of about 4% at 0.35 μm and 9% at 2.5 μm. Relatively strong 1 and 2 μm features due to Fe^{2+} in olivine and pyroxene are present. The

[11] http://nemo.mtholyoke.edu/

2.0 μm position of the pyroxene feature is near the boundary between opx and cpx. A flattening of the spectrum around 1.3 μm additionally indicates the presence of some olivine.

The spectrum exhibits a broad 3 μm absorption that is characteristic of bound water. It is not known how much of the absorption is due to terrestrial contamination versus water in the rock prior to entering the Earth's atmosphere. A small absorption just beyond 6 μm is probably the H–O–H bend in water. Other features in the 5–6 μm region are typical of overtones and combinations from silicate absorptions at longer wavelengths.

A weak absorption at 3.41 μm is observed, characteristic of aliphatic hydrocarbon at the parts-per-thousand level. The feature is short of the position expected for a trace carbonate, and no 4 μm carbonate feature is present. Therefore, trace hydrocarbon is the most likely option. But this hydrocarbon, too, can be terrestrial contamination, including from fingerprints, or could have been present in the rock before it came to Earth.

To evaluate mineralogy, the data were modeled using the B. Hapke (1981) radiative transfer model with extensions for Rayleigh absorption and Rayleigh scattering by small particles (R. N. Clark et al. 2012, 2024). To evaluate the mineralogy of the sample, a first-order fit using available optical constants was obtained with pyroxene and olivine as the main components, with neutral darkening agents using carbon and magnetite (Figure 2, bottom). The magnetite was submicron, imparting a blue slope to the spectrum, but it introduced no spectral features. The feldspar abundance and grain size had little effect on the model except for brightness. An increase in feldspar abundance would increase reflectance, requiring an increase in carbon abundance to lower the reflectance to maintain the match. To first order, abundances of olivine and pyroxene could be changed with a proportional change in grain size with similar close fits; thus, the specific abundances and grain sizes are not unique because the spectral features are weak. The pyroxene optical constants used also do not exactly match the observed 1 and 2 μm pyroxene band positions. The pigeonite (from USGS spectral library 07; R. F. Kokaly et al. 2017) had slightly longer absorption band positions than in the Hamburg spectra. Additional optical constants for the pyroxene composition series are needed to make a better fit. Despite these limitations, the analysis matches both the pyroxenes and olivine.

The spectrum of the powder (not shown) had similar spectral properties as seen in the slab but higher noise, making uncertain some interpretations of the presence of phyllosilicate features in the 2.2–2.3 μm region. The slab spectrum, with its higher signal-to-noise ratio, showed that there are no detectable phyllosilicates in that spectral region. The slope from the 0.7 μm reflectance maximum to the 1.4 μm maximum was +0.003 in the powder and −0.016 in the slab. Both of these slopes are "bluer" than they would be in the case of slopes created by pyroxene and olivine. Thus, both powder and slab spectra require a "bluing" agent, which is created by fine-grained particles (R. N. Clark et al. 2012). The slab shows stronger pyroxene and olivine absorption than the powder spectra by 50% greater band depth. This is to be expected. The slab has the most grains in contact, so that there are fewer mineral–air (or vacuum) interfaces than in the powdered sample. Thus, less scattering occurs in the slab and thus larger effective grain sizes are required in the powder spectrum. The uncertainty in pyroxene abundance is not affected by the wavelength mismatch of the optical constants due to a slightly different pyroxene composition of the optical constants.

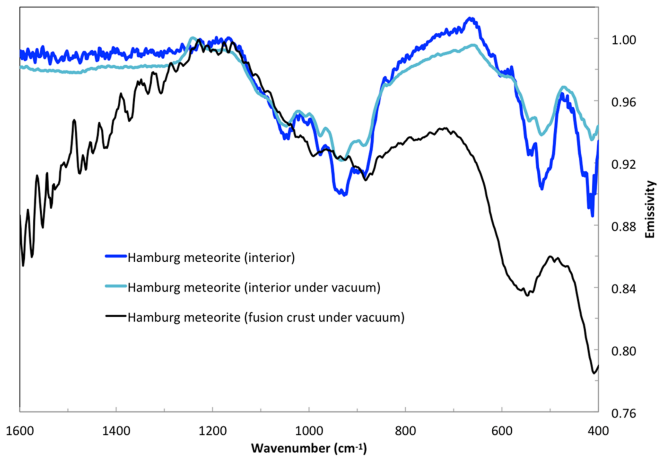

Figure 3. Thermal emissivity spectra of the Hamburg meteorite (Michigan). The interior measurements are shown in blue (ambient pressure) and turquoise (vacuum), and the exterior fusion crust (vacuum) is shown in black.

Three emissivity spectra are shown in Figure 3. To investigate the composition of the meteorite, the ambient pressure meteorite interior emissivity spectrum was analyzed. Using a coarse-particulate spectral library of 58 different rock-forming minerals (Table 1), including a range of feldspar, pyroxene, and olivine compositions, and other mineral classes, the meteorite spectrum was spectrally unmixed over the spectral range of 1700–400 cm^{-1}, according to the linear retrieval algorithm (linear least squares) of M. S. Ramsey & P. R. Christensen (1998), in order to determine the mineralogic composition of the meteorite. The model fit to the laboratory spectrum (Figure 4) indicates that the meteorite sample consists of 64 vol% olivine, 30.4 vol% opx (11.7 vol% enstatite and 18.7 vol% pigeonite), and 5.6 vol% feldspar (albite).

Multiple olivine composition spectra were available in the end-member set; two were coarse particle samples (forsterite AZ-01 and fayalite WAR-RGFAY01), and the 13 samples labeled "Olivine Fo_xFa_y" (Table 1) were synthesized powders pressed into very small pellets to reduce their volume-scattering spectral effects (M. D. Lane et al. 2011). Several olivine compositions were selected for the 1700–400 cm^{-1} spectral unmixing results as follows: 54.5 vol% forsterite (Fo_{100}), 0.6 vol% Fo_{80}, and 8.9 vol% Fo_{50}. These multiple olivine spectral end-members were selected to best fit the meteorite spectrum because the midrange synthetic olivine spectra in the end-member set have some related spectral noise, especially at wavenumbers higher than (shortward of) their Christiansen frequencies (of $\sim$1060 cm^{-1} for fayalite, $\sim$1200 cm^{-1} for forsterite), where the emissivity drops due to uneliminated volume-scattering effects in the pellet spectra (e.g., Figure 4), whereas the Fo_{100} spectrum selected in the spectral analysis is of a coarse sample with clean, deep bands in the spectrum and flatter, higher-emissivity shortward of the Christiansen frequency that are features more similar to the meteorite interior sample spectra shown in Figure 3, lending to it being selected for the model fit. Had the suite of synthetic olivine spectra had cleaner, deeper features, it is likely the Fo_{100} spectrum would not have been the most abundant olivine spectrum chosen but was needed to best fit the overall shape of

Table 1
Listing of the End-member Minerals Used in Spectral Unmixing

Sample Names	
Quartz BUR-4120	K-rich glass
Microcline BUR-3460	Silica glass
Albite WAR-0244	Quenched basalt
Oligoclase BUR-060D	Olivine $Fo_0Fa^a_{100}$
Andesine BUR-240	Olivine $Fo_{10}Fa^a_{90}$
Labradorite WAR-4524	Olivine $Fo_{20}Fa^a_{80}$
Bytownite WAR-1384	Olivine $Fo_{30}Fa^a_{70}$
Anorthite BUR-340	Olivine $Fo_{40}Fa^a_{60}$
Actinolite HS-116.4B	Olivine $Fo_{50}Fa^a_{50}$
Biotite BIR-840	Olivine $Fo_{55}Fa^a_{45}$
Muscovite WAR-5474	Olivine $Fo_{65}Fa^a_{35}$
Chlorite WAR-1924	Olivine $Fo_{70}Fa^a_{30}$
Enstatite HS-9.4B	Olivine $Fo_{75}Fa^a_{25}$
Bronzite NMNH-93527	Olivine $Fo_{80}Fa^a_{20}$
Augite NMNH-9780	Olivine $Fo_{89.5}Fa^a_{10.5}$
Augite NMNH-122302	Olivine $Fo_{100}Fa^a_0$
Hedenbergite DSM-HED01	Orthoclase WAR-RGSAN01
Serpentine HS-8.4B	Oligoclase WAR-5804
Serpentine BUR-1690	Pigeonite (syn. $Wo_{10}En_{36}Fs_{54}$)
Forsterite AZ-01	Diopside WAR-5780
Fayalite WAR-RGFAY01	Antigorite NMNH-47108
Hematite BUR-2600	Ca-montmorillonite STx-1 solid
Anhydrite ML-S9	Magnesiohastingsite HS-115.4B
Gypsum ML-S6	Magnesiohornblende WAR-0354
Calcite ML-C27	Hypersthene NMNH-B18247
Dolomite ML-C28	Pyrite ML-SD
Nontronite WAR-5108 granular	Troilite ML-I9
Fe-smectite SWa-1 solid	Wollastonite BUR-5080
Illite IMt-2 granular	Anorthoclase WAR-0579

Note.
[a] Synthetic olivine spectra from M. D. Lane et al. (2011); otherwise, the spectra are from the Arizona State University spectral library (P. R. Christensen et al. 2000) or coauthor M.D.L.'s collection.

the meteorite spectrum over the full 1700–200 cm^{-1} range. Nonetheless, the spectral unmixing results suggest that the olivine in the meteorite is clearly dominated by a high-Mg-content olivine.

However, when the meteorite spectrum is compared to individual olivine spectra, the Fo_{80} spectrum best matches specific identifiable features. In Figure 3, the Fo_{80} synthetic olivine spectrum is shown in addition to the meteorite spectrum and the model fit (Table 2). The Fo_{80} spectrum features at 977.8 and 835 cm^{-1} match well to the meteorite spectrum. Furthermore, the emissivity maxima in the meteorite spectrum at 579.9 cm^{-1} and the peak position centered at ~469 cm^{-1} are best matched to the Fo_{80} olivine (M. D. Lane et al. 2011).

The other olivine compositions in the end-member suite have bands that are not at these locations, thus indicating the olivine in the Hamburg meteorite to be ~Fo_{80}.

It is interesting to note that the major phase abundances determined in the MIR are the reverse of those found in the VNIR. In the VNIR, opx with an intermediate composition ("hypersthene") is the major phase at 46%, following by "pigeonite" (low-Ca) at 33% and low- and high-Mg olivine at 11% and 2%, respectively. In the MIR where mineral mixing is linear and therefore less complicated to unmix, the estimated abundances are 64% high-Mg olivine and 30% opx (modeled as enstatite) and pigeonite (12% and 19%, respectively).

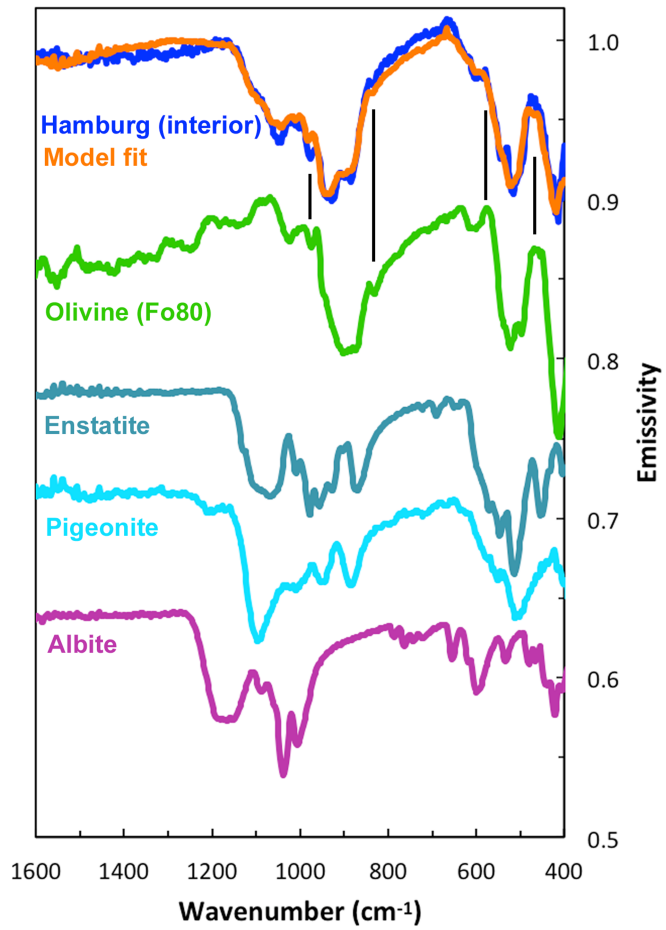

Figure 4. The blue spectrum is the measured sample, while the orange spectrum is the model fit (shown with rms value in Table 2). Mineral spectra used in the model fit are shown below the meteorite. The green spectrum is synthetic olivine (Fo_{80}; M. D. Lane et al. 2011), dark turquoise is enstatite, light blue is pigeonite, and purple is albite. Mineral spectra are offset for clarity. Vertical lines are drawn at several wavelengths to emphasize features in the meteorite that are due to Fo_{80} olivine.

Table 2
Minerals Selected for the MIR Spectral Unmixing Analysis of the Interior (Ambient Pressure) and Estimated Abundances

Mineral	Abundance by Species (volume %)	Abundance by Mineral Group (volume %)
Olivine (Mg-rich)	…	64.0
Forsterite (Fo_{100})	54.5	…
Fo(80)	0.6	…
Fo(50)	8.9	…
Pyroxene	…	30.4
Enstatite	11.7	…
Pigeonite	18.7	…
Feldspar (albite)	…	5.6
Serpentine	…	1.1
Total (rms = 0.57%)	…	101.1

Note. Volume percentages <5 may be unreliable.

We noted above that the VNIR model fits are not unique. By changing the grain size of a component, the abundance in the model fit will change. The accuracy of the optical constants in the VNIR models is also not known. The presence of fine

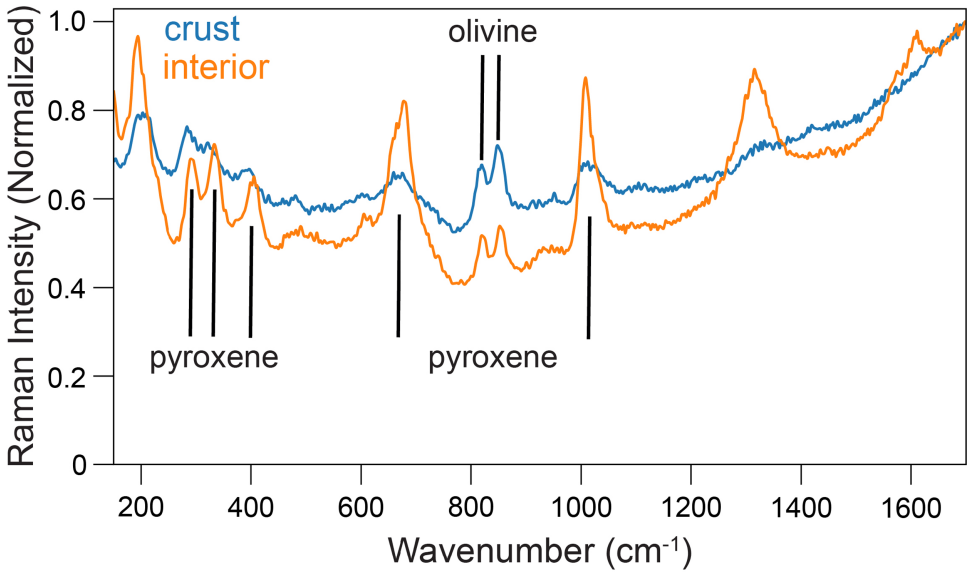

Figure 5. Normalized Raman spectra of the interior (orange) and crust (blue) of the Hamburg meteorite.

particles can also influence the MIR spectra, resulting in changes in abundances.

5.2. Raman

Diagnostic bands within these spectra indicate the presence of both olivine (~820, 852 cm^{-1}) and pyroxene (~678, ~1008 cm^{-1}) (Figure 5). The lack of features from 450 to 515 cm^{-1} indicates that feldspar minerals were not detected within the powdered samples.

In addition to mineral group identifications, mineral species can be estimated using preestablished Raman spectroscopy calibration models. Overall, Raman spectroscopy is a better technique compared to many other spectroscopy methods for estimating mineral species compositions, provided that a Raman calibration model exists. For example, using the equation $\%Fo = -0.179625x^2 + 310.077x - 133717$ (where x = DB2 centroid in units of cm^{-1}), the olivine forsterite percentage (%Fo) of the sample can be determined (L. B. Breitenfeld et al. 2018). From this method, the %Fo is estimated to be roughly 82 ± 4 vol%.

In cases where Raman spectroscopy calibration models for mineral groups are lacking the spectral pattern, the peak position of specific Raman features can provide general compositional information. Determining pyroxene species composition in meteorites is especially complex as multiple species can be present, resulting in overlapping spectral features. A. Wang et al. (2001) detail a flowchart for distinguishing Raman pyroxene mineral species using Raman spectroscopy. The interior meteorite spectrum contains a merged doublet feature at ~678 cm^{-1} (with a shoulder toward smaller wavenumber values) in addition to three pyroxene features at ~292, ~333, and ~407 cm^{-1}. These observations are consistent with a *Pbca* mineral like enstatite or a $P2_1/c$ mineral like pigeonite. Additionally, the pyroxene feature(s) centered on average near ~670 cm^{-1} shifts to higher wavenumbers with lower Fe content or the percentage of ferrosilite (L. B. Breitenfeld & M. D. Dyar 2020), indicating that the Hamburg pyroxene has low Fe content.

A. Wang et al. (2001) also provide the following general equation for determining pyroxene composition:

$$n_i = a_i X^{\mathrm{Mg2+}+b_i X^{\mathrm{Fe2+}}+c_i X^{\mathrm{Ca2+}}},$$

where n_i is a function of the frequency (cm^{-1}) of the Raman peaks at $a_i \approx 1000$ cm^{-1}, $b_i \approx 670$ cm^{-1}, and $c_i \approx 1000$ cm^{-1} and $X^{\mathrm{Mg2+}}$, $X^{\mathrm{Fe2+}}$, and $X^{\mathrm{Ca2+}}$ are the molar ratios of Mg^{2+}, Fe^{2+}, and Ca^{2+} in octahedral sites where $X^{\mathrm{Mg2+}} + X^{\mathrm{Fe2+}} + X^{\mathrm{Ca2+}} \leqslant 2.0$. However, A. Wang et al. (2001) find that both Fe and Ca cause peak shifts in the same direction at about 1000 cm^{-1}, and thus this equation produces less accurate results when the a_i peak at ≈1000 cm^{-1} is used. A more useful set of predictive equations results from use of the second and third peaks from above:

$$n_2 = a_i X^{\mathrm{Mg2+}+c_i X^{\mathrm{Ca2+}}+d_i},$$

$$n_3 = a_i X^{\mathrm{Mg2+}+c_i X^{\mathrm{Ca2+}}+d_i},$$

where d_i is an intercept. The resultant equations using their recommended coefficients are

$$n_2 = 31.9 X^{\mathrm{Mg2+}-7.7 X^{\mathrm{Ca2+}}+655},$$

$$n_3 = 51.7 X^{\mathrm{Mg2+}+20.5 X^{\mathrm{Ca2+}}+297.3.}$$

Note that the VNIR model fit also required two pyroxene compositions in order to match the broad 2 μm Fe^{2+} pyroxene absorption width.

For the Raman spectrum of the meteorite interior, the relevant peaks occur at 678.5 and 333.18 cm^{-1}. Solving these equations predicts a pyroxene composition with negative (−0.07) Ca cations pfu and an Mg of 0.72 cations pfu, within the error bars they provide. From this, we infer an average composition for pyroxene in this meteorite of $Mg_{0.72}Fe_{0.28}Ca_0$. Given that P. R. Heck et al. (2020) reported both cpx and opx in this sample, this composition is probably a mixture of the different phases. More detailed Raman microanalysis of pyroxenes would likely discriminate the two phases with different compositions, but the Raman spectra of the powdered interior and fusion crust splits can at this point only be interpreted as mixtures.

In addition to mineralogical Raman features, the Raman spectrum of the interior of the sample contains first-order D and G carbon bands at ∼1314 and ∼1609 cm^{-1} (Figure 5). These Raman features are useful in understanding the thermal history of the meteoritic material using carbon thermometry (e.g., investigations of ordinary chondrites; H. Busemann et al. 2007; G. D. Cody et al. 2008; E. Quirico et al. 2009; N. A. Starkey et al. 2013; Y. Homma et al. 2015; J. M. Young 2021). These spectral features are offset to different wavenumber values than typical features within similar meteorites (e.g., J. M. Young 2021). To perform a robust Raman organic thermometry estimate for the Hamburg meteorite, additional data are needed. Raman spectroscopy is a spectroscopic technique particularly useful for studying the composition and history of insoluble organic matter.

As for abundances, Raman spectroscopy is not an ideal technique for quantifying the relative proportions of minerals because different Raman scattering cross sections (inherent Raman signal strength) of different minerals complicate mineral abundance quantification. The Raman spectra of the Hamburg meteorite were acquired from a powdered sample; therefore, it acts as a mixture of minerals. The strong pyroxene features combined with the intrinsically lower Raman cross section of pyroxene group minerals compared to olivine (L. B. Breitenfeld et al. 2025) suggest that a high proportion of pyroxene is present relative to olivine. This is again consistent with the VNIR results.

L. B. Breitenfeld et al. (2025) developed two mineral quantification techniques using Raman spectroscopy including multivariate models and Raman cross-section proxies. The multivariate model predicts 30.5 vol% olivine and 82.2 vol% pyroxene, whereas the Raman cross-section proxy method estimates 5.8 vol% olivine and 94.2 vol% pyroxene. It should be noted that the multivariate modeling predictions of olivine and pyroxene are derived independently with two separate models. This differs from the Raman cross-section proxy method values that are estimated through a single equation, are interdependent, and are forced to add to 100 vol%. Additionally, the Raman cross-section proxy value for enstatite is considerably lower (0.19) compared to other pyroxene samples (e.g., 0.49 for diopside and 0.61 for augite; L. B. Breitenfeld et al. 2025). If the enstatite Raman cross-section proxy value is in fact underestimated, a higher value would result in lower pyroxene abundance predictions that would be more aligned with the multivariate estimates.

5.3. Mössbauer

Spectra of the meteorite taken from the interior and the fusion crust are remarkably similar (Figure 6; Table 3). This may reflect that bulk samples were used and the fusion crust actually contained significant material from the interior underneath. The spectra are dominated by the sextets arising from Fe metal and Fe carbide, both common phases in metal-bearing meteorites including chondrites (A. N. Krot et al. 1997; M. L. Hutson et al. 2016; J. I. Goldstein et al. 2017; R. F. Muftakhetdinova et al. 2018; A. J. Brearley 2021). Because this technique looks only at Fe atoms and the peak intensities are proportional to the abundances of Fe in each phase and site, there are no peaks arising from feldspar or phases in which the total percentage of Fe atoms is <1%.

The technique of Mössbauer spectroscopy is not generally used to estimate the composition of phases because mixtures

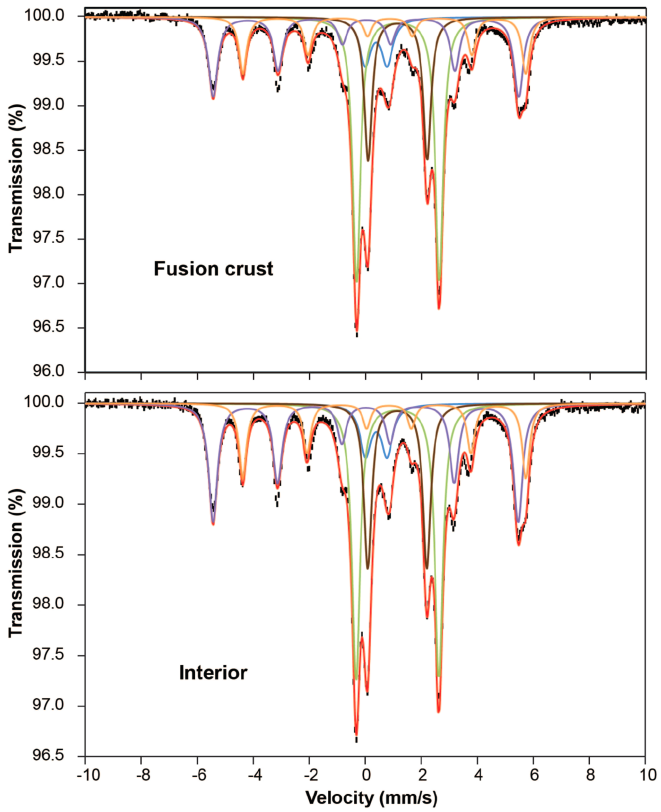

Figure 6. Mössbauer spectra of the fusion crust (top) and interior (bottom) of the Hamburg (Michigan H4) meteorite. Sextets are assigned to Fe in metal (purple) and Fe carbide (orange). Doublets correspond to Fe^{3+} in pyroxene (blue) and Fe^{2+} in olivine + pyroxene (green) and pyroxene (brown).

affect the ability to fit peak positions accurately, and in many cases, there is no peak shift with composition. Such interpretations are only possible when exhaustive background work has been done to carefully study subtle changes in composition (if they occur). For example, it is possible to get some indication of olivine composition by comparing to the study of synthetic olivine with variable composition by M. D. Dyar et al. (2009) and data from the thesis by E. C. Sklute (2006). In general, olivine spectra are best represented by fits with two doublets with the same value of δ (about 1.15 mm s^{-1}) and $\Delta \approx 2.80$ and 2.84 mm s^{-1} arising from Fe mixed in the M1 and M2 sites, such that M1 and M2 cannot be distinguished using Mössbauer. In spectra like those of the Hamburg meteorite, the overlap of the olivine peaks with those from pyroxene makes such detailed fits impossible; a composite olivine/pyroxene doublet with $\delta = 1.15$ mm s^{-1} and $\Delta = 2.96$ mm s^{-1} is observed. Matching the Hamburg parameters to those in Table 4.2 of E. C. Sklute (2006) and assuming that pyroxene does not perturb the olivine peaks suggests that the best parameter match of the Hamburg olivine is to synthetic samples with Fo_{60} to Fo_{70}. A higher Δ value of about 2.99 or 3.00 mm s^{-1} would be characteristic of Fo_{80} and Fo_{90}, respectively.

Similarly, shifts in Mössbauer peak position are observed for different types of pyroxene (M. D. Dyar et al. 2007, 2013). In this meteorite study, the overlapped doublet with quadrupole splitting of 2.96 mm s^{-1} is not diagnostic of any specific pyroxene composition due to overlap with olivine, but the doublet at $\Delta = 2.14$ mm s^{-1} is a match to high-Mg opx ($En_{97.5}$) in two-doublet fits (M. D. Dyar et al. 2007 2013).

Table 3
Mössbauer Parameter for Fusion Crust and Interior

Sample	Center Shift (mm s^{-1})	Quadrupole Splitting (mm s^{-1})	Line Width (mm s^{-1})	Hyperfine Field (T)	Area	Assignment
Fusion crust $\chi^2 = 3.10$	0.37	0.78	0.48	…	9	Fe^{3+} pyroxene
	1.15	2.95	0.33	…	34	Fe^{2+} in olivine and pyroxene
	1.14	2.11	0.33	…	18	Fe^{2+} in pyroxene
	0.02	−0.02	0.39	338	25	Fe metal
	0.76	−0.20	0.33	313	15	Fe carbide
Interior $\chi^2 = 3.51$	0.39	0.76	0.48	…	8	Fe^{3+} pyroxene
	1.15	2.96	0.24	…	30	Fe^{2+} in olivine and pyroxene
	1.14	2.11	0.33	…	18	Fe^{2+} in pyroxene
	0.02	−0.01	0.38	338	29	Fe metal
	0.76	−0.17	0.31	313	16	Fe carbide

Finally, we note that there is little difference in peak areas between the sample with fusion crust and the interior one, for two likely reasons. First, Mössbauer is inherently a volume technique, and the ratio of surface area to interior in this sample may not be large enough for the fusion crust to show up. Second, although Mössbauer features arising from glass tend to have broad peak shapes, their energies are still dependent on the observed valence state and coordination polyhedra of the Fe atoms in the sample. In this case, these are superimposed on the peaks arising from the other phases and therefore cannot be separately resolved.

5.4. Image Analysis

To compare against the mineral abundances obtained by the different spectroscopic techniques, we also sought to analyze the phases present using image analysis. The paper by P. R. Heck et al. (2020), as discussed earlier, provides thorough petrographic characterization of these meteorites, including two composite red, green, and blue Energy Dispersive Spectroscopy maps of two entire slices of the type section (their Figure 5(b) and 10 bottom) and numerous close-ups of chondrules (their Figure 7). The ImageJ software was used to convert each map to an 8 bit image. The threshold tool was then used to determine the percentage of the image that corresponded to the phase of interest.

As an example, Figure 7 (upper left) uses a map of a porphyritic olivine with pyroxene (POP) in a chondrule from P. R. Heck et al. (2020). For this map in that paper, the element Mg was coded red, Ca was green, and Al was blue. Because olivine does not contain Ca or Al, the highest-saturation red was assigned to olivine (this paper, Figure 7, top left; 26%), while the low red saturation peak was assigned to pyroxene (this paper, Figure 7, top right; 30%). In this map, this method is not able to distinguish other phases (blue/green in mapped image) from the pyroxene due to their same color properties in the 8 bit image. However, these are easily observed and optically quantified in the colored element maps. For this chondrule, analysis suggests that, after removing all black voids and veins, 48% of the chondrule consists of olivine and 52% consists of pyroxene (+blue/green phases).

Applying this technique to the two larger, full slice element maps in P. R. Heck et al. (2020) illustrates the heterogeneities that are encountered in different sections of this meteorite. For the section labeled "Hamburg 1," pyroxene/feldspar (80%) clearly dominates (olivine = 19%), as seen in the middle row of our Figure 7. For "Hamburg 2" (bottom row of Figure 7), a subequal amount of olivine and pyroxene (+feldspar) is observed (51% olivine, 47% pyroxene/feldspar).

5.5. Spectral Matching and Classification

The results of matching the Michigan H4 spectra from Figure 2 against the meteorite and asteroid databases are shown in Figure 8. It is worth mentioning that our VNIR data were recorded from a slab, while the meteorites are a mix of slabs and particulate samples, and the asteroids are, of course, of unknown surface textures. However, the matching algorithm appears to see through the texture effects to a large extent and find matches that make sense, as follows.

Meteorite matches are to one H4 (Tysnes Island), one LL5 (NWA438), two L4 (Barratta and Rupota), and three H5 (Beardsley, Barwise, and Cangas de Onis) meteorites. All these groups should be spectrally similar because they contain varying proportions of olivine and pyroxene and so are dominated by those features. H group meteorites contain roughly equivalent amounts of those two phases, the L group has slightly more olivine, and LL group samples have a lot more olivine than pyroxene. Although it contains roughly twice as much olivine as pyroxene, the Michigan H4 sample has been independently classified, likely on the basis of its abundant chondrules and homogenized olivine compositions. This matching algorithm can be termed successful in that it correctly identifies highly similar samples as matches.

The asteroid matches also show prominent olivine and pyroxene features. The lower panel of Figure 8 shows the best matches to these data, which comprise the L/H/LL/URE, EH/EL/AUB, and CO/CV asteroid classes as defined by M. D. Dyar et al. (2023) based on classification models trained on meteorites. As noted above, the first of these combined groups contains absorption features due to olivine and pyroxene representing a continuum between varying amounts of olivine and pyroxene. So L/H/LL/URE is an entirely appropriate type of asteroid to match. The EH/EL/AUB class spectra are generally featureless, but those meteorites typically also contain low-Ca pyroxene, forsterite, and feldspar. Finally, the CO/CV class has similar mineralogy, though the spectra generally have weaker absorption features. However, Figure 8 shows the close resemblance of the A007763 and A0085989 asteroid spectra to that of Michigan H4.

Limited information on the location of the parent body can also be obtained from understanding the spectrum of Michigan H4. The M. D. Dyar et al. (2023) paper ranks its eight classes on the basis of semimajor axis length, with HED (Vesta) group asteroids shortest and IAB/IIAB and CM/C2/CR meteorite analogs being

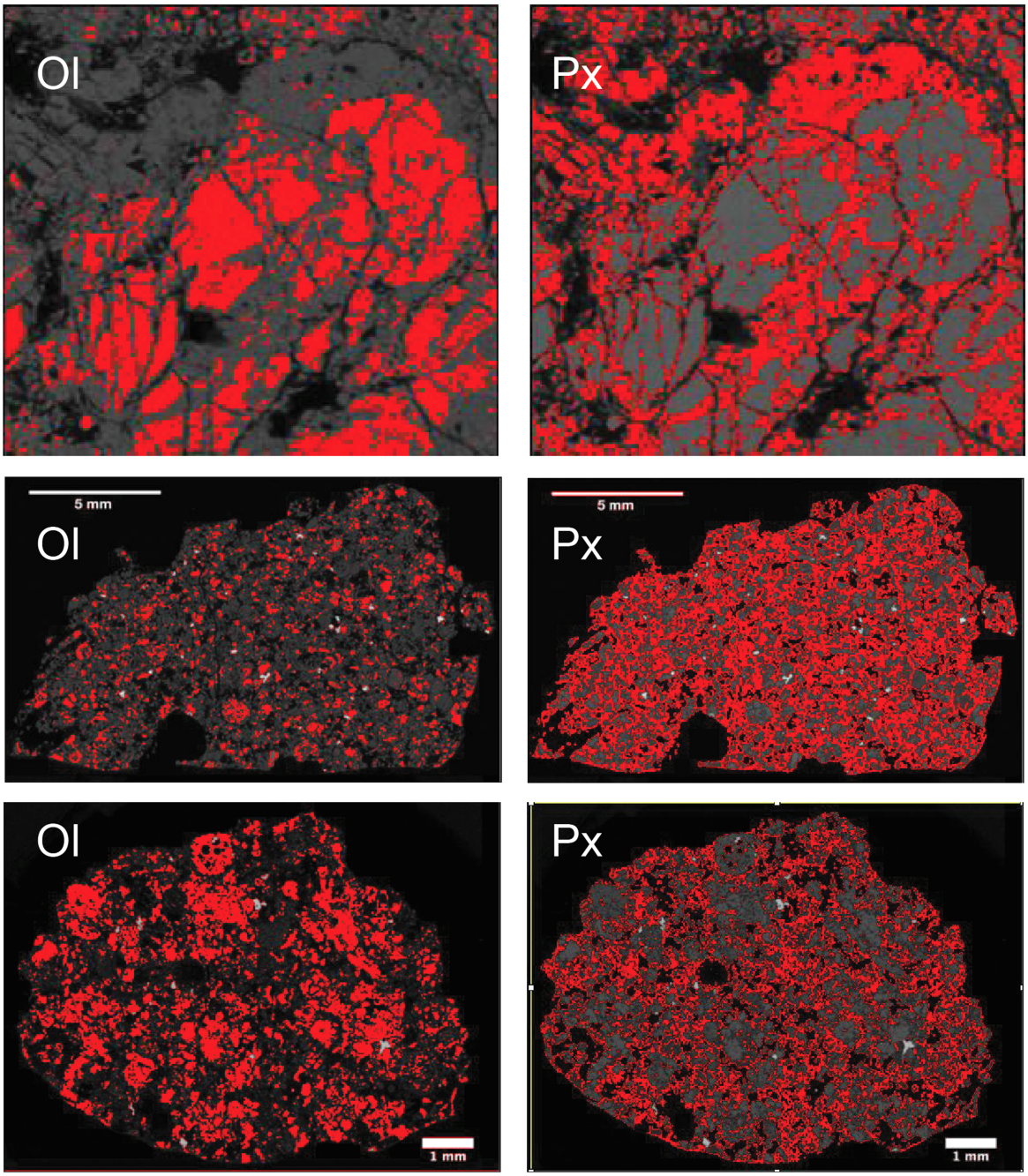

Figure 7. Images of the Hamburg meteorite reprocessed using ImageJ to threshold olivine (left) and pyroxene (right) so as to estimate their abundances. The saturated red color in all images is olivine, while the darker red is pyroxene. (Top) Close-up of a chondrule map from P. R. Heck et al. (2020; their Figure 7, upper left image). (Middle) Slice of the Hamburg type sample ME6108.3 from P. R. Heck et al. (2020; resampled from their Figure 5(b)). (Bottom) A second slice through the type sample ME6108.3, resampled from P. R. Heck et al. (2020; their Figure 10, bottom).

the longest. On that scale, the three groups of matches are intermediate in semimajor axis lengths (excluding Mars-crossing and near-Earth objects, which have perturbed orbits).

6. Discussion

6.1. Mineral Mode Comparisons among Techniques

Synthesis of our methods reproduces the prior microprobe examinations of the Hamburg meteorite, showing that it consists of high-Mg olivine (forsterite) accompanied by low-Ca pyroxene (enstatite and/or pigeonite) and Na-rich (low-Ca) feldspar (oligoclase) (Table 4).

The mineral modes of this meteorite are predicted comparably by VNIR and Raman unmixing with pyroxene > olivine by a ratio of 79:13 and 82–94 to 6–3, respectively. Note that these values are given in wt%, not vol%. In contrast, unmixing in the MIR shows an opposite trend of pyroxene to olivine of 30:64. The presence of feldspar ranges from 2.9 wt% (by VNIR) to 5.6 vol% (MIR). These low values explain the lack of detection by Raman and Mössbauer. Only 1.1 vol% of serpentine is estimated from the

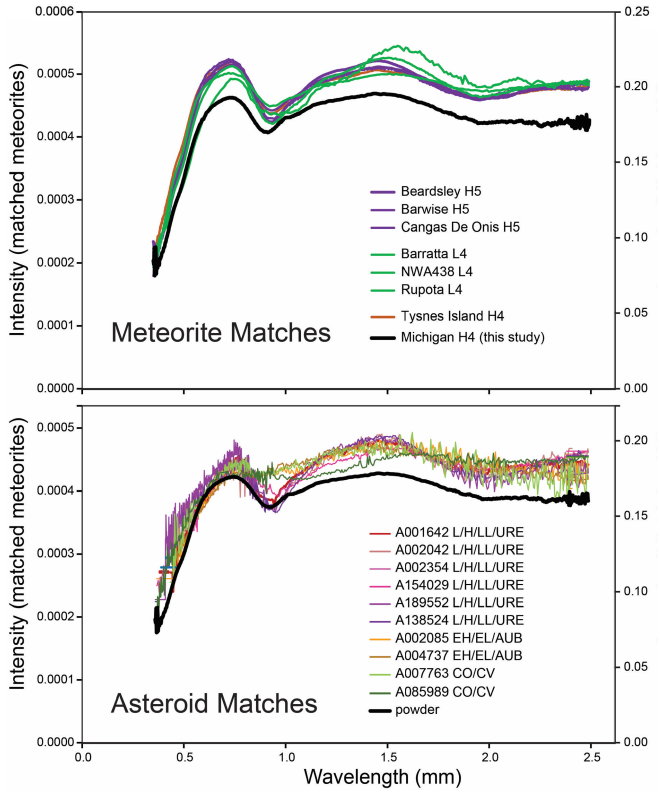

Figure 8. Results of matching the Michigan H4 meteorite spectra to the meteorite and asteroid spectral libraries collected by M. D. Dyar et al. (2023).

MIR data, though the OH fundamental band is not detected at 2.7 μm (see Figure 2).

The lack of agreement among methods is attributed to the heterogeneity in this specific meteorite, as seen in Figure 7. The H4 class of ordinary chondrites is named on the basis of relatively high Fe contents (thus the "H"). The type 4 designation refers to the abundance of chondrules and the presence of homogeneous olivine compositions indicative of equilibration by lower-grade thermal metamorphism. T. L. Dunn et al. (2010) included six H4 chondrites in their detailed comparison of olivine (Ol) to pyroxene (Px) ratios using X-ray diffraction and spectral data. In that study, the ratio of Ol/(Ol+Px) ranged from 0.46 to 0.54. This result is consistent with one of the slices studied by Heck et al. (bottom row of our Figure 7) but not the other (middle row), for which this ratio would be 0.19.

It is important to note that the ratio of olivine to pyroxene in this class is not prescribed by the H4 definition per se. Indeed, both P. R. Heck et al. (2020) and other studies have subsequently documented that it is common for H-class meteorites to be heterogeneous at varying scales. For example, R. H. Jones et al. (2016) observed widely varying apatite compositions in Zag H3–6 breccias and inferred that the parent body was heterogeneous. A. Kimura et al. (2002) reported heterogeneous distributions of refractory inclusions in H3 chondrites. In the Hamburg sample, P. R. Heck et al. (2020) analyzed the mean compositions of the phases present and the differences between matrix and chondrites discerned by petrography and found them to be consistent with a classification of H4, S2, W0. This was further confirmed by their Cr and O isotopic analyses.

With respect to the lack of consensus among the unmixing methods in this paper, it is also important to note that the measurements reported here were all done on varying parts of the meteorite. It is likely that different measurements (one slab for VNIR, a different slab for MIR, and interior and fusion crust powders made from the latter slab by Raman) all had different populations of minerals given the complexity of this sample. The sample is composed of a fairly typical mix for an ordinary chondrite of chondrules, metal blebs, porphyritic olivines, and ground mass containing both olivine and pyroxene. The techniques used here sampled different parts of the meteorite and illustrate the complexity of estimating mineral abundances. So, unfortunately, this heterogeneity of mineralogy means that our unmixing methods cannot be validated.

6.2. Olivine and Pyroxene Compositions

Olivine composition as determined by MIR, Raman, and Mössbauer is uniformly indicated to be high in Mg. In the VNIR model, the depression of the reflectance in the 1.3 μm region requires a high-iron olivine and thus the F029 component. Thus, the VNIR model fit indicated 11 wt% Green Sand Beach olivine, Fo_{89}. The MIR and Raman analyses specify a nearly identical composition of $Fo_{80–82}$, and the less specific Mössbauer analysis indicates an olivine of $Fo_{60–70}$ composition (but peak overlapping makes it difficult to pinpoint). Although our specific sample was not the same as that used in P. R. Heck et al. (2020), our results are very similar because all the rocks in the Hamburg meteorite fall likely were once part of a larger specimen that broke apart upon entry. The P. R. Heck et al. (2020) analysis measured olivine with an average of $Fo_{81.3\ \pm 0.7}$, a composition that falls beautifully between our MIR and Raman values and not far from the Mössbauer and VNIR estimates.

Pyroxene compositions were identified using VNIR, MIR, Raman, and Mössbauer spectroscopies. In the VNIR, the broad 2 μm pyroxene band is broader than a single composition, thus the need for two significantly different pyroxene compositions in the model. Both VNIR and MIR detected both cpx and opx: VNIR predicted 33.2% pigeonite and 45.9% enstatite, while MIR unmixing finds 18.7% pigeonite and 11.7% enstatite. In contrast, the Raman and Mössbauer techniques each produced a single estimate for the average pyroxene composition with $En_{72}Fs_{28}Wo_0$ and $Fs_{2.5}$, respectively. The findings of P. R. Heck et al. (2020) determined the pyroxene composition to be close to ferrosilite, with a composition of $Fs_{16.3\pm0.4}Wo_{1.3\pm0.1}$.

The significance of knowing the olivine and pyroxene compositions lies in their petrogenetic implications. As magmas cool and evolve, the compositions and ratios of minerals change (as idealized by Bowen's reaction series). For typical cooling magmas, one of the first minerals to crystallize is high-Mg olivine, such as the olivine identified in the Hamburg meteorite ($Fo_{80–82}$), indicating limited igneous differentiation prior to its formation. The modal abundances of high-Mg olivine, low-Ca pyroxene, and minimal plagioclase feldspar (at ~64, ~30.4, and ~5.6 vol%, respectively, as modeled using the MIR data) and the visual characteristics of the meteorite (i.e., the presence of chondrules) all indicate that Hamburg is appropriately classified as an H4. Ordinary chondrites, of which the H4 class is a subdivision, are typical of ~80% of all terrestrial falls (T. Burbine 2017).

Table 4
Comparison of Analytical Techniques Used

Phase	VNIR	MIR	Raman	Mössbauer	P. R. Heck et al. (2020) EMPA
Olivine	13.2 wt%	64.0 vol%; Fo_{80}	5.8–30.5 vol%; Fo_{82}	$Fo_{60} - Fo_{70}$	$Fo_{81.3 \pm 0.7}$
Enstatite	45.9 wt%	11.7	82.2–94.2 vol%; $En_{72}Fs_{28}Wo_0$	$Fs_{2.5}$	$Fs_{16.3 \pm 0.4}Wo_{1.3 \pm 0.1}$
Pigeonite	33.2 wt%	18.7	82.2–94.2 vol%; $En_{72}Fs_{28}Wo_0$	$Fs_{2.5}$	$Fs_{16.3 \pm 0.4}Wo_{1.3 \pm 0.1}$
Albite	2.9 wt%	5.6	n.d.	n.d.	$An_{14.0 \pm 4.0}Ab_{81.1 \pm 3.0}$ $Or_{4.8 \pm 1.3}$
Serpentine /bound water	…	1.1	n.d.	n.d.	n.d.

6.3. Feldspar and Nonsilicates

The Raman and Mössbauer spectroscopies could not detect any feldspar because of low Raman cross sections of the feldspar and because Mössbauer is sensitive only to Fe, which is very low in feldspar. However, the VNIR and MIR emissivity spectra indicated the presence of some albite. Its low-Ca abundance agrees with the low-Ca composition of the detected feldspar of $An_{14.0\pm4.0}Ab_{81.1\pm3.0}$ $Or_{4.8\pm1.3}$ (oligoclase) in P. R. Heck et al. (2020).

Mössbauer is the only technique used here that sheds light on the presence of nonsilicate phases in Michigan H4. In both the fusion crust and sample interior, the Mössbauer parameters indicate that Fe metal and Fe in a carbide phase are present: 25%–29% in metal and 15%–16% in carbide, respectively. Note that these abundances, expressed as percentages of the total Fe present, are not modal abundances, as are being determined by the other spectroscopic techniques in this study.

7. Conclusions

This study combines results from techniques that are used both on remote (VNIR and MIR) and in situ (VNIR, SWIR, Mössbauer, and Raman) applications. As in prior studies (e.g., C. M. Pieters et al. 2008; M. D. Dyar et al. 2009), the value of using integrated methods to understand complex samples is amply demonstrated. Although it is sometimes necessary to use results from a single technique or observation, the resultant conclusions of such studies may be biased by experience from previous data and lead to incorrect assumptions in a new setting (C. M. Pieters et al. 2008). It is critical to always consider the varying scales and depths of measurement. For example, Mössbauer is a bulk technique in which gamma rays pass through the sample, whereas reflectance techniques probe only the surface layers and may thus overrepresent surface alteration or coatings on grains. Measurement scales also vary, depending on the instrumentation and its beam size: while Mössbauer is generally a bulk technique, reflectance methods may be implemented on either bulk or microscales. Texture effects such as particle size and surface roughness will also affect reflectance measurements. All of these factors affect how the measurements can be interpreted.

It is clear that all of the techniques used here have strengths and weaknesses, especially when it comes to detecting minor phases. Reflectance methods that excel at understanding silicates (particularly Fe-rich silicates that have spectral features in the VNIR wavelength range) often have difficulty detecting minor phases, especially quartz and feldspar, though hydroxyl-bearing minerals and iron oxides can usually be detected at the 1% level and as parts per thousand or million, respectively. Raman scattering cross sections are often large for covalently bonded phases such as carbides and carbonates, allowing such minerals/phases to be easily detected at very small abundances via Raman. Mössbauer studies excel at detecting minor Fe-bearing oxides and other nonsilicates. It is apparent that optimal analyses from orbit or in situ measurements are obtained using combinations of complementary techniques—a philosophy that was thoroughly embraced by NASA when selecting instrumentation for Martian rovers. Careful consideration of the rock types and likely phases expected on a planetary surface must guide the choice of instrument packages on any mission.

Laboratory methods still provide the most accurate determinations of precise modal mineralogy and geochemistry, but spectroscopy may contribute to such studies by identifying, for example, iron oxides that are key to determinations of oxygen fugacity (Mössbauer) or small amounts of highly covalent carbon (Raman). Finally, the results of this study suggest that spectroscopy (rather than petrography) might provide a "quick and dirty" method for meteorite classification that could be simply done via VNIR or MIR reflectance spectroscopy matched to a meteorite spectral library.

Acknowledgments

This material is based upon work supported by the National Aeronautics and Space Administration through the Solar System Exploration Research Virtual Institute 2016 (SSERVI16) cooperative agreement (NNH16ZDA001N) (TREX).

ORCID iDs

M. Darby Dyar https://orcid.org/0000-0003-4272-793X
Melissa D. Lane https://orcid.org/0000-0003-3264-3337
Timothy Glotch https://orcid.org/0000-0002-8187-3609
Neil Pearson https://orcid.org/0000-0002-0183-1581
Elizabeth C. Sklute https://orcid.org/0000-0001-8980-3798
Amanda J. Hendrix https://orcid.org/0000-0002-0435-8224

References

Binzel, R. P., DeMeo, F. E., Turtelboom, E. V., et al. 2019, Icar, 324, 41
Brearley, A. J. 2021, M&PS, 56, 108
Breitenfeld, L. B., & Dyar, M. D. 2020, LPSC, 51, 1160
Breitenfeld, L. B., Dyar, M. D., Carey, C., et al. 2018, AmMin, 103, 1827
Breitenfeld, L. B., Dyar, M. D., Glotch, T. D., et al. 2025, AmMin, 110, 34
Breitenfeld, L. B., Rogers, A. D., Glotch, T. D., et al. 2021, JGRE, 126, e2021JE007035
Brown, P. G., Vida, D., Moser, D. E., et al. 2019, M&PS, 54, 2027
Burbine, T. 2017, Asteroids: Astronomical and Geological Bodies (1st ed.; Cambridge: Cambridge Univ. Press)
Busemann, H., Alexander, M. O. D., & Nittler, L. R. 2007, M&PS, 42, 1387
Carey, C., Dyar, M. D., Boucher, T., & Mahadevan, S. 2015, JRSp, 46, 894
Christensen, P. R., Bandfield, J. L., Hamilton, V. E., et al. 2000, JGR, 105, 9735
Clark, R. N., Cruikshank, D. P., Jaumann, R., et al. 2012, Icar, 218, 831
Clark, R. N., King, T. V., Klejwa, M., et al. 1990, JRG, 95, 12653
Clark, R. N., Swayze, G. A., Livo, K. E., et al. 2024, PSJ, 276, 48
Cody, G. D., Yabuta, H., Kilcoyne, A. L. D., et al. 2008, E&PSL, 272, 446
DeMeo, F. E., Binzel, R. P., Slivan, S. M., & Bus, S. J. 2009, Icar, 202, 160
Dunn, T. L., McCoy, T. J., Sunshine, J. M., & McSween Jr., H. Y. 2010, Icar, 208, 789

Dyar, M. D., Klima, R. E., Fleagle, A., & Peel, S. E. 2013, AmMin, 98, 1172
Dyar, M. D., Klima, R. L., Lindsley, D., & Pieters, C. M. 2007, AmMin, 92, 424
Dyar, M. D., Sklute, E. C., Menzies, O. N., et al. 2009, AmMin, 94, 883
Dyar, M. D., Wallace, S. M., Burbine, T. H., & Sheldon, D. R. 2023, Icar, 406, 115718
Fries, M., McCubbin, F., Zeigler, R. A., et al. 2019, LPICo, 2157, 6499
Goldstein, J. I., Huss, G. R., & Scott, E. R. D. 2017, GeCoA, 200, 367
Hapke, B. 1981, JGR, 86, 3039
Heck, P. R., Greer, J., Boesenberg, J. S., et al. 2020, M&PS, 55, 2341
Hedlin, M. A. H., Riutsema, J., de Groot-Hedlin, C. D., & Hetland, E. A. 2018, SeisReL, 89, 2183
Homma, Y., Kouketsu, Y., Kagi, H., Mikouchi, T., & Yabuta, H. 2015, JMPeS, 110, 276
Hutson, M. L., Ruzicka, A. M., Farley, K. R., et al. 2016, LPSC, 47, 1377
Jones, R. H., McCubbin, F., , M., & Guan, Y. 2016, AmMin, 101, 2452
Kimura, A., Hiyagon, H., Palme, H., et al. 2002, M&PS, 37, 1417
Kokaly, R. F., Clark, R. N., Swayze, G. A., et al. 2017, U.S. Geological Survey 1035, USGS
Krot, A. N., Zolensky, M. E., Wasson, J. T., et al. 1997, GeCoA, 61, 219
Lane, M. D., Glotch, T. D., Dyar, M. D., et al. 2011, JGRE, 116, E08010
Mitchell, J. L., Fries, M. D., Herd, C. D. K., et al. 2020, LPSC, 51, 2593
Muftakhetdinova, R. F., Brusnitsyna, E. V., & Yakovlev, G. A. 2018, LPICo, 81, 6303
Pieters, C. M., Klima, R., & Hiroi, T. 2008, JGRE, 113, E06004
Quirico, E., Montagnac, G., Rouzaud, et al. 2009, E&PSL, 287, 185
Ramsey, M. S., & Christensen, P. R. 1998, JGRB, 103, 577
Ruff, S. W., Christensen, P. R., Barbera, P. W., & Anderson, D. L. 1997, JGR, 102, 14899
Shirley, K. A., & Glotch, T. D. 2019, JGRE, 124, 970
Shirley, K. A., Glotch, T. D., Donaldson, O., et al. 2023, JGRE, 128, e2022JE007629
Sklute, E. C. 2006, Mössbauer Spectroscopy of Synthetic Olivine Across the Fe-Mg Solid Solution, BA thesis, Mount Holyoke College
Starkey, N. A., Franchi, I. A., & Alexander, C. O. D. 2013, M&PS, 48, 1800
Velbel, M. A. 2014, M&PS, 49, 154
Wang, A., Jolliff, B. L., Haskin, L. A., Kuebler, K. E., & Viskupic, K. M. 2001, AmMin, 86, 790
Young, J. M. 2021, Novel Methods for Investigating Alteration of Airless Bodies, PhD thesis, State Univ. of New York at Stony Brook